Application of adaptive optics in retinal imaging: A quantitative and clinical comparison with standard cameras

E. S. Barriga[1], G. Erry[2], S. Yang[3], S. Russell[4], B. Raman[2], and P. Soliz[2];

[1]The University of New Mexico, Albuquerque, NM, [2]Kestrel Corporation, Albuquerque, NM,
[3]Texas Tech University, Lubbock, TX, [4]University of Iowa Department of Ophthalmology

ABSTRACT

Aim: The objective of this project was to evaluate high resolution images from an adaptive optics retinal imager through comparisons with standard film-based and standard digital fundus imagers. Methods: A clinical prototype adaptive optics fundus imager (AOFI) was used to collect retinal images from subjects with various forms of retinopathy to determine whether improved visibility into the disease could be provided to the clinician. The AOFI achieves low-order correction of aberrations through a closed-loop wavefront sensor and an adaptive optics system. The remaining high-order aberrations are removed by direct deconvolution using the point spread function (PSF) or by blind deconvolution when the PSF is not available. An ophthalmologist compared the AOFI images with standard fundus images and provided a clinical evaluation of all the modalities and processing techniques. All images were also analyzed using a quantitative image quality index. Results: This system has been tested on three human subjects (one normal and two with retinopathy). In the diabetic patient vascular abnormalities were detected with the AOFI that cannot be resolved with the standard fundus camera. Very small features, such as the fine vascular structures on the optic disc and the individual nerve fiber bundles are easily resolved by the AOFI. Conclusion: This project demonstrated that adaptive optic images have great potential in providing clinically significant detail of anatomical and pathological structures to the ophthalmologist.

1. INTRODUCTION

For earlier and more accurate diagnosis of many retinal diseases, information is needed that provides greater spatial resolution views of the retina than is available to the ophthalmologist through direct examination or than is generally achievable with current fundus cameras. The capability for providing the requisite greater detail of retinal structures is possible through the application of advanced imaging technologies such as wavefront sensing of ocular aberrations, correction of these aberrations with adaptive optics [1] , and through image deconvolution techniques. The challenge in meeting the demands for higher resolution retinal images lies in our ability to deal with the aberrations that are introduced primarily by the human eye and which lead to reduced resolution of retinal images. Because of cost and complexity, such a system does not currently exist for clinical use.

In this project we will systematically evaluate the contribution of image deconvolution [2, 3] and wavefront technology [4, 5] in order to quantitate the improvements in retinal image resolution that can be achieved by employing each of these technologies in a low-cost clinical fundus imager. There are three stages of image quality improvements that can be achieved with today's wavefront and adaptive optics technology. Theoretically, the highest resolution is achieved through a sensor with wavefront measurements that is coupled to an adaptive optics mirror which corrects for the measured aberrations. Laboratory (research) systems have been described by Liang and Williams [6], Rhoorda [7], and Miller [8], while a clinical system has been demonstrated by Moscow State University, Larichev [9], and Kestrel investigators, Erry [10], and Soliz [11-13]. These systems, while attractive from a research perspective, are either not suitable for clinical applications [6-8] and/or are currently prohibitively expensive. Kestrel has developed a wavefront sensing-based, adaptive optics fundus imager [9-13] that has been used in pre-clinical studies at Kestrel and Moscow State University since 2002.

1.1 Adaptive optics

Worldwide researchers have shown that adaptive optics techniques can greatly improve the resolving power in astronomical and biomedical imaging. General progress in this field has yielded commercially available components, such as lenslet arrays for wavefront sensors and active wavefront correctors like deformable mirrors. These components form a foundation for the spread of adaptive optics technology into commercial applications. Several groups worldwide are working to apply adaptive optics to ophthalmology using different approaches. A group led by Williams [1, 6]

designed the first adaptive system for retinal imaging based on deformable mirror technology and a Shack-Hartmann sensor. Another group in Spain is well known for developing techniques for eye aberration measurements and coherent adaptive retinal imaging [14]. Rhoorda [7] and Miller [8] also report on devices with similar characteristics.

2. METHODOLOGY

2.1 Adaptive Optics Fundus Imager (AOFI): Description of the AO system

Williams' high-resolution retinal imaging represents the first of its kind. Though in principle the system has been demonstrated to produce cellular-scale resolution, there appear to be several limiting factors to this specific technical implementation that will hamper the development of a commercial clinical device. The first major difference between our AO fundus imager and others' is the field of view (FOV). Our AOFI presents a 15 degree FOV. The clinicians would prefer a wide field of view for their process of screening and detecting possible pathological regions. These other systems, which typically have about a 1degree FOV, are useful in diagnosing focal pathologies, but lack utility in performing a broad search of the retina which is important for detecting and locating pathologies and visualizing lesion margins.

The number of lenslets and actuators for the adaptive mirror affects the costs and complexity of the system. The lenslets are an element of the wavefront sensor that measures the characteristics of the naturally occurring aberrations in the individual human eye. The adaptive mirror corrects for the lower order aberrations using an adaptive optics mirror while the deconvolution post-processing restores lost details resulting from the high order aberrations not corrected by the adaptive optics imaging system. The AOFI in this study uses an 18 element bimorph mirror that is relatively lower in cost that those commonly used by many of the existing laboratory prototypes [6-8]. The adaptive optics imaging system described by Kestrel [9-13] has been designed to suppress low-order aberrations. In order to remove the remaining high order aberrations, image post-processing involving deconvolution is applied by calculating the patient-system optical transfer function (OTF) from the measurements obtained by the Shack-Hartmann wavefront sensor. The evaluation of the relative contribution to the correction of ocular aberrations by the adaptive optics mirror and the deconvolution methodology is one of the aims of this paper.

2.2 Deconvolution methods: Point Spread Function (PSF) deconvolution and blind deconvolution

Some investigators have reported on the successful application of deconvolution techniques to astronomical images. An approach that combines wavefront measurement technology, adaptive optics, and image deconvolution algorithms has been shown to significantly improve image quality [15].

Imaging of the retina in the presence of aberrations from the eye and additive noise encounters the same problem that has challenged astronomy: imaging of stars in the presence of atmospheric aberrations and noises. In astronomy, the use of adaptive optics (AO) has enabled considerable progress toward correcting for the effects of atmospheric aberrations. Image processing such as image deconvolution has also been part of the solution to correcting distortions and obtaining clear images of stars. The same strategy can be used to capture retinal images.

The goal of image deconvolution is to restore an image from its degraded form to an image that more closely approximates its original unaberrated form.

2.3 Wavefront-based deconvolution methods

The OTF can be computed through the direct measurement of the ocular aberrations, i.e. the wavefront measurement using the Shack-Hartmann wavefront sensor, represented in the form of recorded Zernike coefficients. The wave aberration expressed as the summation of a set of Zernike polynomials is given by

$$W(x,y)=\sum_{i=0}^{n} C_i Z_i(x,y)\,, \tag{1}$$

where $W(x,y)$ is the wavefront, C_i the Zernike coefficient of Zernike polynomial $Z_i(x,y)$. In the experimental set up of this project, the number of Zernike modes is up to n=25. The OTF can be expressed as the autocorrelation of the pupil function $P(x,y)$,

$$OTF(u,v) = \int\int P(x,y)P(x-u,y-v)dxdy,$$
$$\widetilde{H}(u,v) = OTF(u,v), \tag{2}$$

where the pupil function is computed from the reconstructed wavefront $W(x,y)$,

$$P(x,y) = \exp\left[\frac{2\pi}{\lambda}W(x,y)\right], \tag{3}$$

and λ is the Shack Hartmann operating wavelength.

After $\widetilde{H}(u,v)$ is obtained, the image can be restored by direct deconvolution from Wiener filtering or pseudo-inverse filtering.

Let $S_n(u,v)$ the power spectrum of the noise, while $S_I(u,v)$ the power spectrum of the image. With Wiener filtering, we have

$$\widetilde{F}(u,v) = \frac{G(u,v)\widetilde{H}^*(u,v)}{|\widetilde{H}(u,v)|^2 + \alpha\frac{S_n(u,v)}{S_I(u,v)}} = \frac{G(u,v)\widetilde{H}^*(u,v)}{|\widetilde{H}(u,v)|^2 + \frac{\alpha}{SNR}} \tag{4}$$

where $G(u,v)$ is the Fourier Transform of the distorted image and α is a scaling parameter and SNR the signal to noise ratio of the imaging system. When the noise characteristics of the system are not available, the image can be restored using a simpler form, the pseudo-inverse filter, given by

$$\widetilde{F}(u,v) = \frac{G(u,v)\widetilde{H}^*(u,v)}{|\widetilde{H}(u,v)|^2 + k}, \tag{5}$$

where *k* is a parameter that controls the sharpness of the restored image. When *k* is small, the edges in restored image are sharp but noisy. For image values of *k* the image are less sharp, but the noise in the image is reduced.

2.4 Blind Deconvolution (BD) methods

Blind deconvolution estimates both the system transfer function $\widetilde{H}(u,v)$ or PSF $\widetilde{h}(x,y)$ and the image $\widetilde{f}_{final}(x,y)$ simultaneously without specific information about the imaging system or the image. There are numbers of existing BD methods [16, 17]. However, most of the methods assume certain degradation models or are optimized towards certain image modality. For those approaches without parametric models the deconvolution is iterative in nature and suffers from stability issues and is computationally intensive. In this project, the goal is to optimize existing deconvolution methods towards retinal image restoration and develop BD methods with fast processing speed, high efficiency and no operator interaction. The preliminary results show that Self-deconvolving Data Reconstruction Algorithm (SeDDaRA) [18] is one candidate for this application.

SeDDaRA is a computationally efficient, non-iterative algorithm. It requires no operator interaction. Neither does it require knowledge of $H(u,v)$. The algorithm assumes a shift-invariant and real degradation model,

$$H(u,v) = K_G \mathbf{S}\{|G(u,v) - N(u,v)|\}^{\alpha(u,v)}, \tag{6}$$

where S{ } is a smoothing operator, α(.) is a tuning parameter within (0,1), K_G is a positive scalar chosen such that |H(u,v)| <1. The frequency dependent power parameter α(u,v) is given by

$$\alpha(u,v) \approx \frac{\log[K_G S\{|\, G(u,v)\,|\}] - \log[K_{F'} S\{|\, F'(u,v)\,|\}]}{\log[K_G S\{|\, G(u,v)\,|\}]}, \tag{7}$$

where F'(u,v) is a true image (a clear, perfect reference image) of the same type as the image being restored, K_G and $K_{F'}$ are determined such that $|H(u,v)|<1$. With F'(u,v), the image can be recovered by

$$\widetilde{F}(u,v) = \{K_G S\{|\, G(u,v)\,|\}\}^{\alpha(u,v)}. \tag{8}$$

For most of the image restoration cases, frequency dependent α is difficult to obtain because of the lack of a referencing true image and also the singularities in Equation (8). In our application a perfect reference image is not possible to obtain. The perfect image can be estimated using an aberration-free image with similar frequency characteristics of the high resolution retinal image. However, this is also a difficult and time-consuming task. Therefore, in spite of the belief that a frequency dependent α would yield better restoration of the image, it is not a likely solution for this application. To circumvent the problem, the possibility of adopting a constant α was studied. If the frequency spectrum of an image peaks at a very narrow range of low frequency and then rapidly falls off with a flat tail at high frequencies, then the spectrum can be approximated by power law with constant α. In this case, a constant α instead of a frequency dependent α is sufficient for restoration and enhancement of the high frequency components, which is lost in image formation and is the cause of blur. Fortunately, the retinal image power spectrum shows this desirable property, as an example is illustrated in Figure 1. In this example, α was approximated with a value between 0.10 and 0.30.

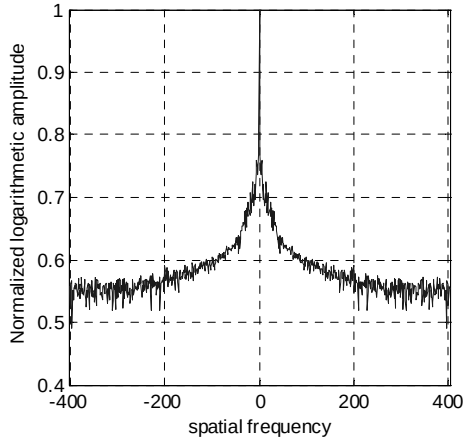

Figure 1. Power spectrum of a retinal image.

2.5 A Description of image quality metrics used for the comparison of the modalities

Image quality assessment on a perceptual level remains the domain of the human expert. Defining robust metrics for image quality is still an intensely researched area. It is broadly accepted in medicine that the human visual system is quite proficient at determining relative image quality and is usually applied comparing two images. Most of the existing techniques, whether used in perceptual applications or quantitative ones, are fidelity-based metrics rather than quality measuring metrics. To assess the improvements offered by the adaptive optics and the deconvolution techniques, metrics were implemented that are thought to be related to human perceptual qualities and could provide a quantitative means for evaluating the images.

The quantitative metrics that were used are those related to gray-level distribution, frequency content, and contrast. The gray-level distribution was measured by entropy [19]. Frequency and contrast were also thought to be related to the visual criteria that human perception system uses to evaluate the quality of an image. Intuitively, an image with higher measured contrast should be perceived by the human to have better quality than one with lower contrast. Similarly, sharper edges will result in higher spatial frequency and should be perceived by the human observer to have better image quality.

The mean and standard deviation gives us an idea of the histogram properties. Shannon's entropy will give a measure of the randomness of an image and is calculated by:

$$H(X) = -\sum_i P(X = x_i) \log_2 P(X = x_i) \tag{9}$$

The entropy as calculated by the previous equation will be measured in bits. A low value of entropy means small amounts of variation in the image and therefore poor contrast. Higher values mean better contrast but can also mean a higher amount of noise in the image.

The spatial frequency indicates the overall activity level in an image. For an image with M rows and N columns the row and column frequencies are calculated by

$$Row\_freq = \sqrt{\frac{1}{MN}\sum_{j=0}^{M-1}\sum_{k=0}^{N-1}\left[f(j,k)-f(j,k-1)\right]^2} \tag{10}$$

and

$$Col\_freq = \sqrt{\frac{1}{MN}\sum_{k=0}^{N-1}\sum_{j=0}^{M-1}\left[f(j,k)-f(j-1,k)\right]^2} \tag{11}$$

The total spatial frequency is then calculated by

$$Spatial\_freq = \sqrt{(row\_freq)^2 + (col\_freq)^2} \tag{12}$$

The contrast was obtained using Haralick's method laid out in [20]. The contrast is a measure of variations in the texture of the image. An increase in the contrast means a better perception of details in the image.

The equation for contrast is given by,

$$Contrast = \sum_{i=1}^{N_g-1} n^2 \left\{ \sum_{\substack{i=1 \\ |i-j|=n}}^{N_g}\sum_{j=1}^{N_g} p(i,j) \right\} \tag{13}$$

where $p(i,j)$ is the (i,j) entry in the normalized spatial grey level dependence matrix, N_g is the number of distinct grey levels in the image. An image with a shadow covering a wide area will have a lower contrast value compared to an image with large grey level variations in it.

2.6 Human subject testing

Human subject testing was approved by the University of New Mexico Health Sciences Center's Institutional Review Board, IRB HRRC 01-398. Informed consent was obtained from each of the participants in the study.

Three subjects were selected for imaging on the AOFI. Images of the posterior pole and optic disc were obtained through a broad band green filter. The 3072 by 2048 pixel format digital camera captured an image of approximately 15 degrees FOV. The spatial resolution of the AOFI is approximately 3 micrometers. To provide a basis for comparison of the AO images, standard color film-based images were obtained with a Topcon TRC50 camera. The color film was digitized at 50 pixels per mm. The green channel was used for the inter-modality comparisons. Digital retinal images were also collected with a Zeiss FF5 fundus camera with a 30 degree FOV. An Apogee AP9E 14 bit depth digital camera fill the FOV with 960 by 720 pixels.

3. RESULTS

In this section we compare the images from the three subjects and the three cameras. For each subject we will present the original images, the processed ones and the statistics calculated in each case.

3.1 Subject X1

Subject X1 is a 60 year old male, Hispanic, with no known retinal or system disease. For this subject we will focus on the left eye's optic disc and will present the quantitative metrics from the adaptive optics images that resulted after processing with the PSF deconvolution and the blind deconvolution methods. A quantitative comparison of the color image and the AO image accompanies each qualitative discussion of the perceptual differences in the three image modes. Figure 2(a) shows a region of interest, ROI, (990 by 1120 pixels) which represents only one-third the area of the original image. Each of the ROIs is further scaled to 22 percent of the original image for purposes of presentation on the page. Figure 2(b) is the result of the application of the blind deconvolution processing with the α parameter set to 0.3.

Figure 2(c) is the result of the deconvolution based on the point spread function. The ROIs are approximately 2400 micrometers wide. The human optic disc is typically 1500-1700 micrometers in diameter.


(a)


(b)


(c)

Figure 2. Optic Disc images for subject X1. (a) Original adaptive optics image. (b) The adaptive optics image after blind deconvolution with parameter α=0.3. (c) The adaptive optics image after processing using the PSF deconvolution.

Image Statistics	Original	Blind Deconvolution	Point Spread Function
Entropy	11.8	14.8	14.9
Spatial Frequency	438	2215	1061
Contrast	2.1	39.1	10.9

Entropy is based on a 16-bit image.

The blind deconvolution processing (b) brings out the fine vessels on the disc with much more clarity than the PSF-based deconvolution. The fine vessels are especially pronounced on the temporal (right) side of the optic disc. Striations emanating from the optic disc in (b) are likely to be a result of the nerve fiber bundles. The higher spatial frequency and higher contrast of the image processed with the blind deconvolution is consistent with the perceived higher image quality of this image.

3.2 Subject S5

Subject S5 is a 42 year old Caucasian male, who was diagnosed with type I Diabetes Mellitus (DM) 18 years ago. Today, this patient was found to have mild background diabetic retinopathy. In this example, three different modalities are presented in Figure 3: (a) digitized standard color film (green channel only), (b) standard (non-AO) digital (green filter), (c) original adaptive optics (green filter), and (d) the adaptive optics image with blind deconvolution. An area of neovascularization is marked with an ellipse (200 by 300 microns in dimension). The finer vessels that compose the neovascular net are 3-4 pixels in diameter or about 8-10 micrometers. It is worth noting that this lesion was not detected

by direct examination by an ophthalmologist and is not identifiable as neovascularization in the image derived from the film (a), often mentioned as the gold standard in ophthalmic imaging. The magnification of the film through the digitization process (50 pixels per mm) captures the grain in the film and results in a noisy image. The standard digital camera (b) does depict the area of neovascularization as well as a number of microaneurysms (indicated by the arrows). However, the details of the neovascular net are absent. The blind deconvolution was applied to the AO image (c); resulting in (d). There is a significant improvement in the details present in the deconvolved AO image when compared to the original AO image.

Table 1 presents the calculated metrics for each of the images shown in Figure 3. There is a general increase in contrast and spatial frequency as one goes from (a) to (d), where (d) is the AO image processed with the blind deconvolution. The contrast and spatial frequency appear to correlate well with the visual impression of image quality.

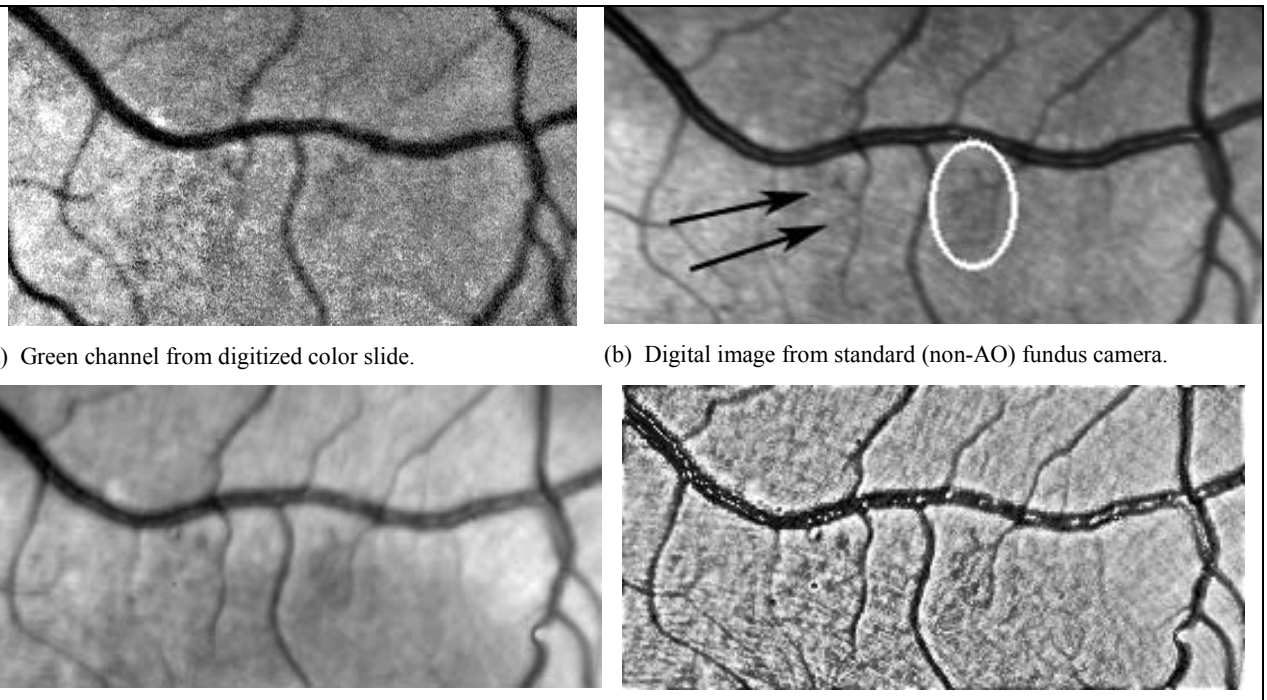

(a) Green channel from digitized color slide.

(b) Digital image from standard (non-AO) fundus camera.

(c) AO image without deconvolution

(d) AO image processed with blind deconvolution, □ = .0.4.

Figure 3. Subject S5 Neovascularization (inside the ellipse in (b), about 200 by 300 micrometers in dimension), as presented by the three different images modalities. Arrows in (b) point to two microaneurysms. The images increase in perceived detail. The deconvolved AO image in (d) is the only image that shows the tree-like structure of the neovascularization. It is also the only image where the nerve fiber bundles are visible (flowing from the left to the lower right). The microaneurysms to the left of the neovascularization are easily discerned in this image.

Table 1. Statistics for the images in Figure 3.

Image	(a) Color (12bits)	(b) Standard digital	(c) AO original	(d) AO with BD α=0.4
Entropy	5.3	7.2	6.4	14.0
Spatial Freq.	7493	3024	2767	5170
Contrast	98.0	86.8	81.7	247.0

3.3 Subject S6

Subject S6 is a 58 year old Caucasian female with bilateral age-related macular degeneration. She presents with drusen in both eyes. Ten years prior to these images, S6 was diagnosed with Type II Diabetes Mellitus (DM) and for this study presented with background diabetic retinopathy (BDR). Two modalities were available for comparison: standard color slides (green channel digitized at 50 pixels per mm) and AO images of the posterior pole. For the left eye, a comparison between the color images (green channel) and the AO images before and after BD is presented. Two regions of interest

are presented. In Figure 4, the images of the optic disc are given. A region essentially covering the fovea is shown in Figure 6.

Figure 4(a) shows the digitized green channel from the color slide for the first ROI (the optic disc). Figures 4(b) and (c) show the AO images before and after BD for the optic disc. Note that there is significant improvement in resolution that is achieved by the AO images. The larger vessels appear to have sharper edges in both of the AO images, (b) and (c). On the optic disc, the fine vascular network can be seen best in the deconvolved image (c).

(a) Green channel from digitized color slide.

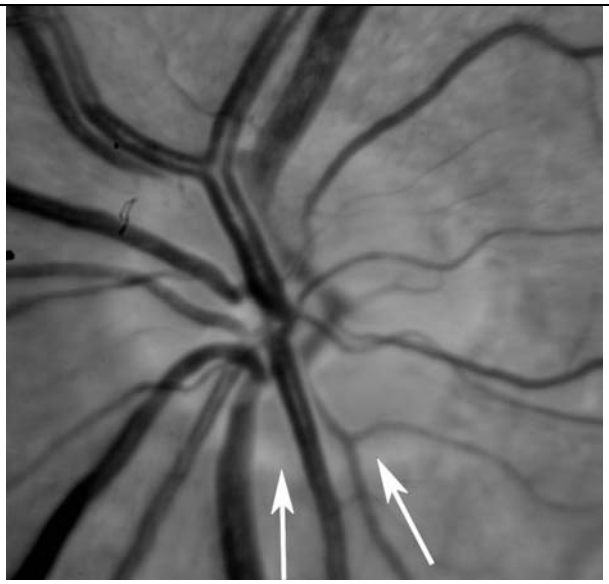

(b) AO image before processing.

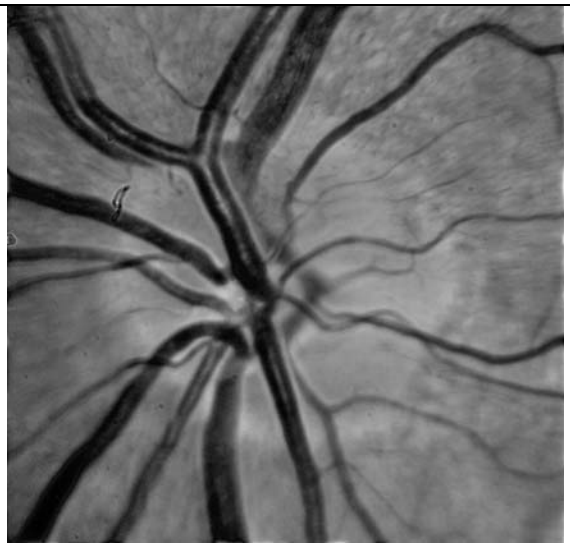

(c) AO image processed with a blind deconvolution.

Figure 4. The optic disc for Subject S6. Arrows on (b) mark the start and end of an intensity cross section shown in Figure 5. The intensity cross section is given to illustrate the sharpness of the edges of the two vessels.

Image Statistics	Green	Original AO Image	Deconvolved AO Image
Entropy	6.6	6.8	7.1
Spatial Frequency	2.3	3.7	12.8
Contrast	3.6	7.9	85.2

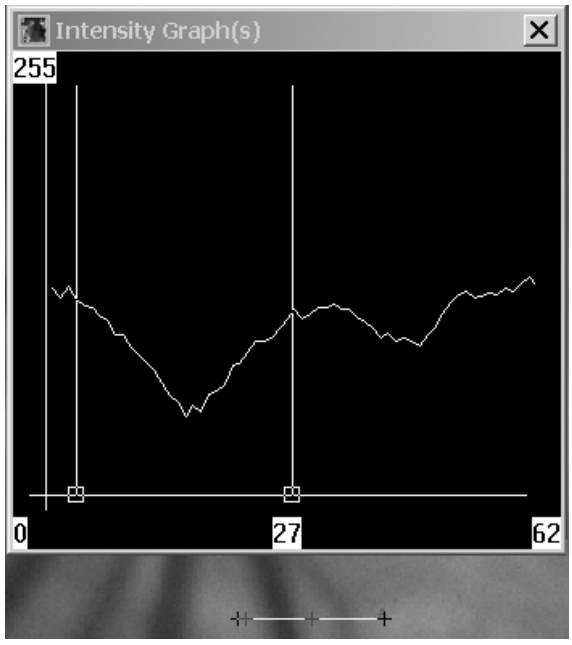

(a)

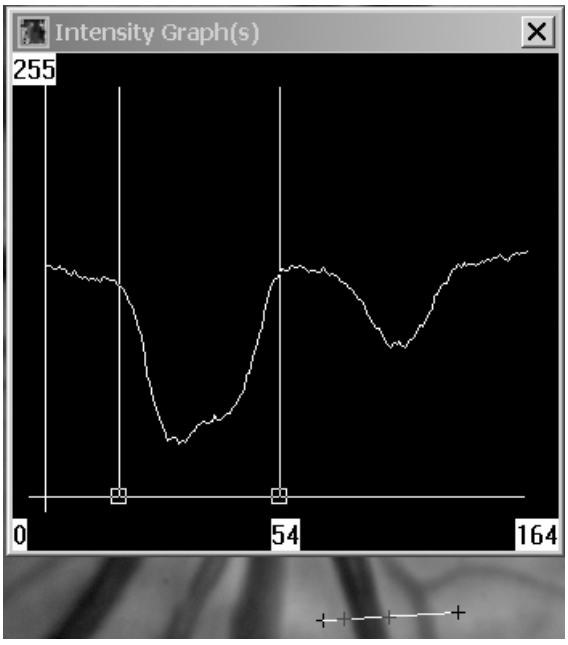

(b)

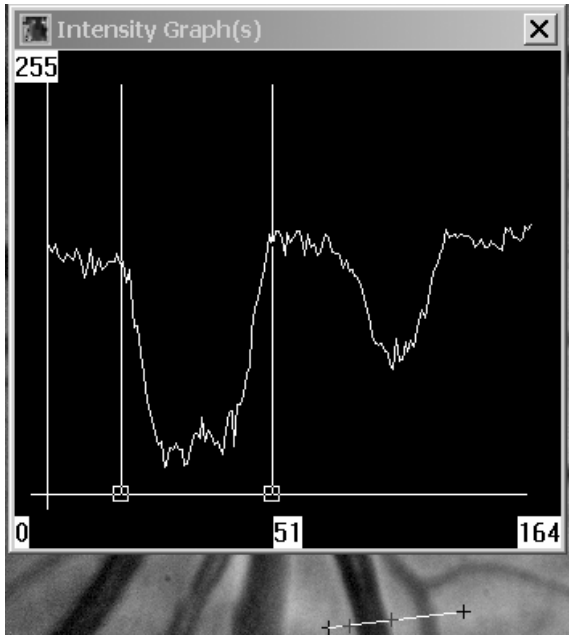

(c)

Figure 5. Intensity cross section of the segment through the inferior part of the optic disc along the rim margin, as marked by the arrows in Figure 4b.

Note the flatness of the edges in the green channel (a) of the digitized color image (between the vertical lines). The edges are much sharper in the AO image (b), as indicated by the larger difference between the surrounding disc tissue (outside the vertical lines) and the interior of the vessel (inside the vertical lines). The edge sharpness is greatest for the deconvolved image (c). However, the noise has also been increased in the image processed by the blind deconvolution (c).

(a) 

(b) 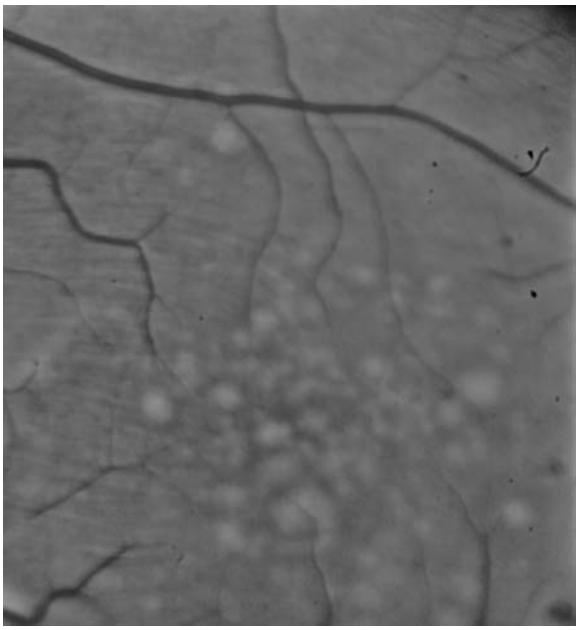

(c) 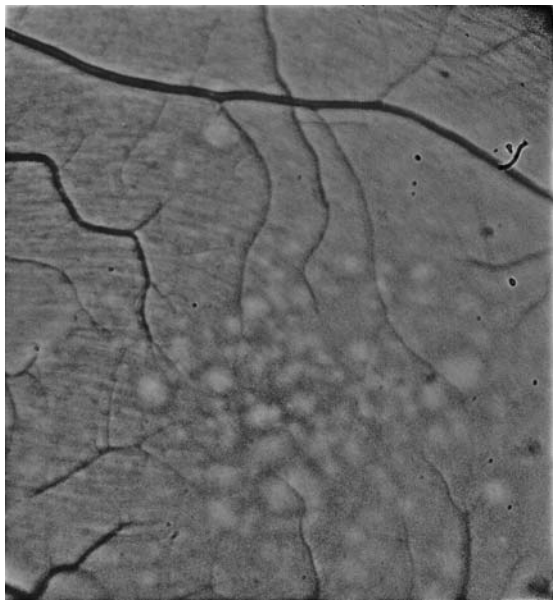

Figure 6(a) shows the color image of the second ROI, which contains the drusen. In Figures 6(b) and (c) we see again the improvement in the quality of the images taken by the AOFI. The image quality metrics for the images are shown below. Note that in this case the statistics have been calculated from the 8-bit version of the images.

Image Statistics	Green	Original	Deconvolved
		AO Image	AO Image
Entropy	6.5	5.3	6.6
Spatial Frequency	7.0	8.0	36.5
Contrast	34.2	32.2	670.2

4. DISCUSSION

A region of interest that focused on the optic disc for Subject X1 was used to illustrate the greatly improved visualization of the details in the fine vascular structures provided by the adaptive optics fundus imager. Figure 2 also demonstrates the further enhancements that can be provided by two techniques for removing aberrations. From this one example, it appears that measuring the aberrations and applying the calculated point spread function offers significant improvement to the image in terms of removing the aberrations. However, the images that result from the blind deconvolution are comparable. The adaptive optics image in Figure 2(b) shows a dramatic improvement over the non-adaptive optics image; as demonstrated by the appearance of the fine vessels on the optic disc. One can also trace the nerve fiber bundles around the disc in both of the deconvolved images. The image produced by the blind deconvolution appears noisier than the image produced using the measured PSF. This may account for some part of the increased spatial frequency and contrast. If one were to increase the power parameter, α, further, then the quality of the image would continue to degrade as the noise would increase.

For Subject S5 three different imaging modalities were presented. The subject has an area of neovascularization that can be easily visualized in Figure 3(d), the deconvolved adaptive optics image. The digitized green channel of the color image exhibits a shadow that can have different interpretations. The high resolution digital image without adaptive optics suggests the presence of the lesion somewhat better than the digitized image in (a). The adaptive optics images without the deconvolution applied, (c), and the deconvolved image (d) leave no doubt regarding the presence of the neovascular lesion. The deconvolution brings out the nerve fiber bundles (d).

For Subject S6, two regions of interest were selected, the optic disc and the central macula. The digitized green channel and the adaptive optics images (with and without deconvolution) are presented for both regions. As with the two previous subjects, the fine vessels on the optic disc are significantly more visible in the adaptive optics images. The deconvolution process further enhances these fine vessels. To demonstrate the increased contrast of the vessels, a cross section of two vessels in the inferior part of the optic disc rim was presented. The difference in contrast among the three images of the optic disc background and the vessel interior is clearly seen in Figure 5. The steeper edge indicates sharper contrast of the vessel wall. It is worthwhile to note the increase in noise in the blind deconvolution over the PSF-based deconvolution. The second region shows a large number of drusen (light patches) throughout the central macula. The drusen edges are greatly enhanced by the adaptive optics images. Additionally, the nerve fiber bundles not commonly seen in standard color retinal photography are clearly seen in Figure 6c, the deconvolved adaptive optics image.

5. CONCLUSIONS

This study presented strong evidence of the potential for deconvolution as a means for removing the blurring effects of ocular aberrations in retinal images. Further investigations will principally focus on refining the deconvolution technique such that the optimal algorithm settings can be automated to provide the highest quality retinal image to the ophthalmologist. The process of identifying the best image quality will be further validated based on the discovery of the quantitative image quality parameters with the highest correlation to the human observer, such as ophthalmologists and trained retinal image readers.

The statistical parameters explored clearly show a relationship to the visual perception of the image quality. However, all the parameters are affected by noise, so that increase in any of these parameters will reflect no only the actual image quality improvement, but also the increase in noise in the image. Further investigation into these and other parameters will lead to the development of a more general image quality metric that can be used as an image quality grading aid for the evaluation of retinal images.

6. REFERENCES

1. Liang, J., Williams, D.R., and Miller, D.T., *Supernormal vision and high resolution retinal imaging through adaptive optics. J.Opt.Soc. Am. A*, **14**(11): p. 2884-2892, 1997.
2. Kundur, D. and Hatzinakos, D., *Blind Image Deconvolution.* IEEE Signal Processing Magazine: p. 43-63, May 1996.
3. Roggemann, M.C., *Limited degree-of-freedom adaptive optics and image reconstruction.* Appl. Opt., **30**(5224-4233), 1991.

4. Fugate, R.Q., Ellerbroek, B.L., Higggins, C.H., Jelonek, M.P., Lange, W.J., Slavin, A.C., Wild, W.J., Winker, D.M., et al., *Two Generations of Laser-guide-star Adaptive Optics Experiments at Starfire Optical Range.* J. Opt. Soc. Am., **11**: p. 310-24, 1994.
5. Otten, L.J. and Larichev, A., *An Ophthalmic Aberrometer for Measuring Aberrations in the Eye.* Patent Application, No. 60/518/274, 7 November 2003.
6. Liang, J. and Williams, D.R., *Aberrations and retinal image quality of the normal human eye.* J. Opt. Soc. Am. A, **14**(11): p. 2873-2883, 1997.
7. Rhoorda, A., *Adaptive Optics Ophthalmoscopy*. Journal of Refractive Surgery 2000, **16**(5): p. 602-607, 2000.
8. Miller, D.T., WIlliams, D.R., Morris, G.M., and Liang, J., *Images of Cone Photoreceptors in the Living Human Eye.* Vision Research, **36**: p. 1067-1079, 1996.
9. Larichev, A., Ivanov, N., Iroshnikov, S., and Gorbunov, M., *Adaptive aberrometer for acuity measurements and testing*. In *To be published in the Proceedings of the 4th International Workshop of Adaptive Optics for Industry and Medicine*, Muenster, Germany, October 19 - 24, 2003.
10. Erry, G., Otten, L.J., Larichev, A., and Irochnikov, N., *A High Resolution Adaptive Optics Fundus Imager*. In *4th International Workshop on Adaptive Optics for Industry and Medicine*, Muenster, Germany, 2003.
11. Soliz, P., Yang, S., Erry, G., Russell, S.R., and Otten, L.J., *The Clinical Utility of High Resolution Images From An Adaptive Optics Retinal Imager*. In *The Association for Research in Vision and Ophthalmology (ARVO), Program #/Poster #: 3032/B667*, Ft. Lauderdale, FL, 2004.
12. Soliz, P., Yang, S., Nemeth, S.C., Erry, G., Russell, S., and Otten, L.J., *The Clinical Utility of High Resolution Images from an Adaptive Optics Retinal Imager*. In *5th International Congress on Wavefront Sensing and Optimized Refractive Corrections*, Whistler, Canada, 2004.
13. Soliz, P., Yang, S., Nemeth, S.C., Erry, G., and Otten, L.J., *Perceived Image Quality Improvements from the Application of Image Deconvolution to Retinal Images from an Adaptive Optics Fundus Imager*. In *4th International Workshop on Adaptive Optics for Industry and Medicine*, Muenster, Germany, 2003.
14. Iglesias, I. and Artal, P., *High-resolution Retinal Images Obtained from Wave-front Sensing.* Optics Letters, **25**(24), December 15, 2000.
15. Christou, J.C., Rhoorda, A., and Williams, D.R., *Deconvolution of adaptive optics retinal images.* J. Opt. Soc. Am., **21**(8): p. 1393-1404, 2004.
16. Ayers, G.R. and Dainty, J.C., *Iterative Blind Deconvolution Methods and its Application.* Optics Letters, **13**(7): p. 547-549, July 1988.
17. Tsumuraya, F., Miura, N., and Baba, N., *Iterative blind deconvolution method using Lucy's algorithm.* Astron. Astrophys., **282**(2): p. 699-708, 1994.
18. Caron, J.N., Namazi, N.M., Lucke, R.L., Rollins, C.J., and Lynn, P.R., *Build data restoration with an extracted filter function.* Opt. Lett., **26**: p. 1164-1166, 2001.
19. Shannon, C.E. and Weaver, W., *The mathematical theory of communication*. 1949, University of Illinois Press: Urbana, IL.
20. Haralick, R.M., Shammigam, K.S., and Dinstein, I., *Textural features for image classification.* IEEE Transactions on Systems, Man, and Cybernetics, **SMC-3(6)**: p. 610-621, 1973.